Toward Non-Invasive Electrical Stimulation for Guided Optic Nerve Regeneration

Pooyan Pahlavan, Peter S. Mayer II, *Graduate Student Member, IEEE*, Anahit Simonyan, Jonathon Cavaleri, Connie Huang, Robert Grady Briggs, Gabriel Zada, Darrin J. Lee, Kimberly K. Gokoffski, and Gianluca Lazzi, *Fellow, IEEE*

***Abstract*— The optic nerve plays a critical role in visual information processing by relaying signals from the retina to the brain. Diseases affecting the optic nerve, such as glaucoma, can severely impair vision due to the nerve's limited capacity for self-repair. One promising approach to promote nerve regeneration involves the use of electric fields to guide axonal growth. Our previous research demonstrated that an electric field applied to the crushed adult rat optic nerve directed full-length axon regeneration and mediated partial restoration of visual function. While effective, this technique involves placing electrodes in direct contact with the optic nerve, posing challenges, including the need for skilled surgeons and the potential for tissue damage during implantation. Leveraging computer simulations and ex-vivo cadaveric measurements, the work in this paper explores noninvasive methods for generating electric fields along the optic nerve. Results show the promise of computational models to correctly estimate the electric fields induced along the optic nerve, providing a platform for designing optimal stimulation systems that will generate fields known to foster axonal growth.**

***Index Terms*— Axonal growth, electrical stimulation, endonasal electrode, computer simulations, electrode placement, electric fields (EFs), ex vivo measurements, cadaveric measurement, neuro-regeneration, noninvasive techniques.**

I. Introduction

THE optic nerve (ON), comprised of retinal ganglion cell (RGC) axons that project to the lateral geniculate nucleus (LGN) in the thalamus and other structures in the diencephalon, plays a critical role in visual information processing. RGC axons enable vision by relaying signals from light-sensitive photoreceptors in the retina to the downstream targets in the brain. Certain diseases of the optic nerve, such as glaucoma, lead to peripheral followed by central vision loss, while other conditions, including metabolic optic neuropathies, cause cecocentral scotomas. Regardless of underlying etiology, vision loss after optic nerve damage is permanent due to RGCs having a limited capacity for self-repair and no capacity for self-regeneration. As such, significant interest exists in developing therapeutic treatments to promote axonal regeneration.

Traditional approaches to drive axonal regeneration within the central nervous system (CNS) have focused on mitigating the diminished regenerative capacity of adult neurons, attributed to a combination of cell intrinsic and cell extrinsic growth-impeding factors. Strategies have primarily centered on reactivating silenced developmental signaling pathways, particularly through targeting of mTOR via PTEN inhibition or SOCS3 inhibition, to revert cells to a growth-permissive state [1], [2], [3], [4]. Despite notable advances, accurately directing regenerating axons to intended targets in the brain continues to pose significant challenges, with frequent reports of stalling or misrouting of RGC axons at critical junctions such as the optic chiasm. Recently, application of electric fields (EFs) has been shown to not only promote axonal growth but also to guide growing axons to their appropriate targets [5]. This suggests that exogenous application of EFs could enable target-specific regeneration within the CNS.

Many modalities of electrical stimulation have been explored as potential treatment for vision recovery. Traditionally, brain computer interfaces have been designed to bypass

Received 11 December 2024; revised 1 June 2025 and 1 July 2025; accepted 28 July 2025. Date of publication 28 August 2025; date of current version 12 September 2025. This work was supported in part by DOD under Grant W81XWH-22-1-0743, in part by NSF under Grant 2121164, in part by the National Institute of Mental Health (NIMH)/NIH under Grant K08MH121757, in part by National Eye Institute (NEI) under Grant P30EY029220, and in part by the Ming Hsieh Foundation and an Unrestricted Grant to the Department of Ophthalmology from Research to Prevent Blindness. *(Corresponding authors: Kimberly K. Gokoffski; Gianluca Lazzi.)*

Pooyan Pahlavan is with the Institute for Technology and Medical Systems (ITEMS) and the Ming Hsieh Department of Electrical and Computer Engineering, University of Southern California, Los Angeles, CA 90089 USA (e-mail: ppahlava@usc.edu).

Peter S. Mayer II is with the Ming Hsieh Department of Electrical and Computer Engineering, University of Southern California, Los Angeles, CA 90089 USA (e-mail: psmayer@usc.edu).

Anahit Simonyan and Connie Huang are with the Department of Ophthalmology, Keck School of Medicine, USC Roski Eye Institute, University of Southern California, Los Angeles, CA 90089 USA (e-mail: anahitsi@usc.edu; huangcon@usc.edu).

Jonathon Cavaleri and Robert Grady Briggs are with the Department of Neurosurgery, Keck School of Medicine, University of Southern California, Los Angeles, CA 90089 USA (e-mail: Jonathon.Cavaleri@med.usc.edu; rgb_326@usc.edu).

Gabriel Zada and Darrin J. Lee are with the Department of Neurosurgery and the Neuro-Restoration Center, Keck School of Medicine, University of Southern California, Los Angeles, CA 90089 USA (e-mail: gzada@usc.edu; Darrin.Lee@med.usc.edu).

Kimberly K. Gokoffski is with ITEMS and the Department of Ophthalmology, Keck School of Medicine, USC Roski Eye Institute, University of Southern California, Los Angeles, CA 90089 USA (e-mail: kimberly.gokoffski@med.usc.edu).

Gianluca Lazzi is with ITEMS, the Ming Hsieh Department of Electrical and Computer Engineering, Alfred E. Mann Department of Biomedical Engineering, and the Department of Ophthalmology, Keck School of Medicine, USC Roski Eye Institute, University of Southern California, Los Angeles, CA 90089 USA (e-mail: lazzi@usc.edu).

Digital Object Identifier 10.1109/TNSRE.2025.3603560

damaged areas (e.g. Argus II to bypass damaged photoreceptors in retinitis pigmentosa) and relay visual information to intact downstream structures (retinal ganglion cells) [6], [7], [8]. Other approaches, such as subretinal and suprachoroidal stimulation devices, are also being explored for similar purposes [9], [10], [11], [12], [13]. Alternatively, Gall et al. [14] presented clinical trial results on repetitive transorbital alternating current stimulation (rtACS) for partially sighted patients with optic nerve damage. Although patients demonstrated improvement in visual field performance, Gall et al. posited that their improvement was likely a result of reactivation of alpha frequency brain activity [14]. Few works, however, directly demonstrate employment of EF for axonal regeneration. A novel intraneural electrode array, OpticSELINE [15], was shown to be an effective stimulator of the optic nerve; rather than directing axon regeneration, however, it is thought to improve vision by bypassing traditional retinal pathways and activating the LGN directly.

Our group has recently demonstrated that application of specific electric fields along a damaged adult rat optic nerve can promote directional axonal growth [16]. Axonal regeneration is hypothesized to be mediated by the targeted EF generated along the ON which drives calcium influx into RGC axons [5], [17], [18]. Although exciting in that these results showed, for the first time, significant directional axonal regeneration, this technique involves implanting electrodes in direct contact with the nerve. Specifically, the approach utilizes a "J-shaped" ("hook") stimulation electrode positioned at the base of the globe around the optic nerve, and a ground electrode implanted intracranially at the contralateral optic tract [19]. This methodology establishes a targeted EF along the ON, which is hypothesized to stimulate and promote axonal regrowth and repair [5], [17], [18]. Direct electrode implantation requires highly skilled surgeons and runs the risk of damaging the optic nerve. As such, we sought to develop noninvasive strategies that would be equally effective at generating an electric field along the optic nerve to promote optic nerve regeneration.

Several parameters can influence the EF induced in a region between two electrodes (stimulation and ground): these include the input current, the dielectrics and tissue between electrodes, the size of the electrodes, and the distance and specific location of the electrodes. In the context of electrical stimulation of biological tissue, there is no opportunity to influence the conductivity between electrodes, which is determined by the tissue conductivity. Therefore, assuming a constant input current, only the physical characteristics and position of the electrodes are degrees of freedom that allow us to influence the EF. Initiating human trials necessitates addressing safety and feasibility concerns, which this study aims to contribute to through computer simulations and ex-vivo measurements. This research explores different stimulation and ground electrodes to find the optimal configuration to generate EF along the optic nerve in humans, comparing implanted to surface electrodes.

In this study, we developed and validated a computational model of electrical stimulation of the human head such that different electrode shapes and positions can be paired and their ability to generate an EF along the anterior visual pathway predicted. This model will help fast-track translational efforts to develop EF stimulation for neural restoration.

II. Methods

A. Cadaveric Conductivity Measurements

The human head is comprised of numerous tissue types, all with varied dielectric properties. When building computational models, such values are usually determined from existing databases (e.g. [20], [21]), which have the advantage of presenting frequency-dependent data in an easily accessible format, often sourced from one or more publications, in a single venue. Although there appears to be consensus regarding dielectric properties of tissues stimulated at high frequencies, large discrepancies exist with low frequency stimulation [22].

Our prior work demonstrated long distance RGC axon regeneration with ultra low frequency (ULF) stimulation (1 KHz) [19]. In other words, the simulations for all practical purposes, can be considered quasi-static. In practice, this means that only the conductivity of the various tissues will impact the induced fields and current distributions in the human head model. Thus, we performed conductivity measurements on cadaveric tissues using the 4-electrode method. This method is widely accepted for low frequency tissue measurement; it also avoids the polarization of electrodes as the sensing and driving electrodes are distinct [23]. To do this, we constructed a probe with 4 platinum electrodes placed 1 mm apart. The probe was calibrated and validated using Phosphate-Buffered Saline (PBS) at various concentrations, and then used to measure the resistance of each tissue at 1 kHz with an E4980A LCR meter (Agilent, Santa Clara, USA).

As our goal was to validate our model against direct measurements performed in cadavers, impedance measurements were performed with cadaveric tissues. Two measurements were conducted for each tissue at different positions within the tissue, then averaged. Two different sets of cadaveric tissue were measured, for a total of four measurements averaged together ($M = 4$). The measured resistances were converted to conductivities as in [24] and the resulting values are provided in Table I. For tissues that could not be measured, such as bone and blood vessels, conductivities provided by IT'IS' low frequency database [25] were utilized. This database is separate from the database based on Gabriel's data [26], and includes tensor imaging data, as well as other newer sources.

B. Electrode Configurations

Provided that the tissue between two electrodes is characterized by uniform and isotropic conductivity, the largest induced EFs are found along a line connecting the two electrodes. This implies that, with implanted electrodes, the optimal location of the electrodes is in direct contact with the optic nerve. Additionally, for a given stimulating current, the closer the electrodes are to each other, the higher the induced EF is.

In considering possible effective locations for non-invasive stimulation of the optic nerve, an electrode placed directly on the cornea (for transcorneal stimulation), resembling a

TABLE I
CONDUCTIVITY OF BIOLOGICAL TISSUES (S/M)

Tissue	IT'IS data based on Gabriel dispersion	IT'IS low frequency conductivity data	Measured data from cadaver	Number of Samples	Coeff. of Variation
White Matter	0.063	0.348	0.185	4	0.481
Gray Matter	0.099	0.419	0.225	4	0.357
Muscle	0.321	0.461	0.512	2	0.362
Fat	0.022	0.077	0.241	4	0.422
Cornea	0.423	0.620	0.722	2	0.367
Sclera	0.505	0.620	0.508	4	0.199
Vitreous Humor	1.500	2.160	1.614	4	0.283
Lens	0.200	0.345	0.382	4	0.250
Optic Nerve	0.029	0.348	0.569	4	0.039

contact lens, is a convenient option [27], [28], [29]. This location is advantageous as the electrode is close to the optic nerve without interposed bone, which is a poor conductor. Furthermore, an electrode positioned on the cornea can be aligned coaxially with the optic nerve. While achieving perfect coaxial alignment is not precisely attainable, this general alignment allows for the potential to generate a maximal EF distribution along the longitudinal axis of the optic nerve. The contact lens electrode considered for this purpose is a single-turn ring of 6 mm outer radius and 5 mm inner radius.

Designing a noninvasive ground electrode is challenging as there is no location on the human head that is on the same axis of the optic nerve, without interposing bone. Although extracephalic ground montages show advantages compared to cephalic montages in the context of brain stimulation [30], and this montage is used in vision restoration [14]], based on prior simulations the optimal location for the ground plate electrode is on the scalp, over the occipital bone. This location aligns with the optic nerve, facilitating the desired directional stimulation. The ground electrode considered here was modeled as a conductive square plate of size 16 cm^2.

Simulations of noninvasive electrical stimulation of the optic nerve were compared to traditional implanted electrodes. Electrodes considered were those used to drive RGC axon regeneration in rats [16], scaled up to fit the human head. The source electrode was modeled as a 30 mm "J-shaped" stimulation electrode placed around the optic nerve at the base of the eye, while the ground as a 10 mm straight needle electrode placed in the contralateral optic tract.

Additionally, we wanted to investigate the use of an endonasal electrode. This electrode consists of an "L-shaped" coated wire electrode, with metallization exposed for 10 mm at the end of the wire and placed along the ON near the orbital apex. The electrode is located between the J-shaped electrode and the intracranial electrode and can be used as either stimulation or ground. We hypothesized that adding such electrode could strengthen the EF along the optic nerve.

C. Quasistatic Computational Modeling

Given the low frequency of the treatment (1 KHz), quasistatic approximations are adequate for an accurate assessment of the current distribution within the tissue [32], [33], [34]. This approximation allows us to forego the inclusion of inductive effects. Further, our primary interest in the current patterns within the tissue allows us to neglect capacitive effects, which are present at the electrode-tissue interface and are only essential to characterize transients – an aspect that is not a priority for our analysis. Thus, to maximize the computational efficiency of the numerical method, we have considered only the conductivity for each of the tissues, as in [35], [36], [37], [38].

The quasistatic method that we employed relies on a multiresolution version of the Admittance Method (AM), a computational method developed by our group [29], [32], [39], [40]. The AM, is a numerical technique for analyzing electromagnetic fields under a quasistatic approximation. At its core, the multiscale AM uses a voxelized grid of admittances to represent the resistivity and permittivity of tissues within a computational model.

This method involves partitioning the problem space into homogeneous domains, each with a known conductivity (σ). This partitioning creates an equivalent electrical network. For a 3D model with cuboid voxels, the admittance value for an edge along the $\hat{x}$ direction, g_{i,j,k_x}, is approximated by:

$$g_{i,j,k_x} = \sigma_{i,j,k} \frac{\Delta y \Delta z}{\Delta x} \tag{1}$$

Here, Δx, Δy, and Δz are the lengths of the edges in the $\hat{x}$, $\hat{y}$, and $\hat{z}$ directions, respectively. The resulting electric network is expressed as a linear system:

$$GV = I \tag{2}$$

In this equation, G is the admittance matrix, V is the voltage vector, and I is the current vector. External stimulation, often from a time-varying magnetic field or a current source, is introduced into the V or I vectors. The currents and voltages within this network, and thus at all points in the computational model, are calculated considering the specific source(s), ground(s), and stimulation current. Solving this system yields the unknown scalar variable (voltage or current), from which the electric field can be reconstructed. A significant advantage of the AM is its ability to incorporate new electrical components into the equivalent circuit, allowing for the modeling of complex bioelectrical phenomena.

The Mida model (see Fig. 1), which is a heterogeneous human head model of 0.5 mm resolution was the computational head model of choice because it provides a faithful representation of the human head, encompassing the eyes, ears, and deep brain structures, along with numerous distinct muscles, bones, skull layers, arteries, veins, cranial nerves, and salivary glands [31]. However, as we planned to validate

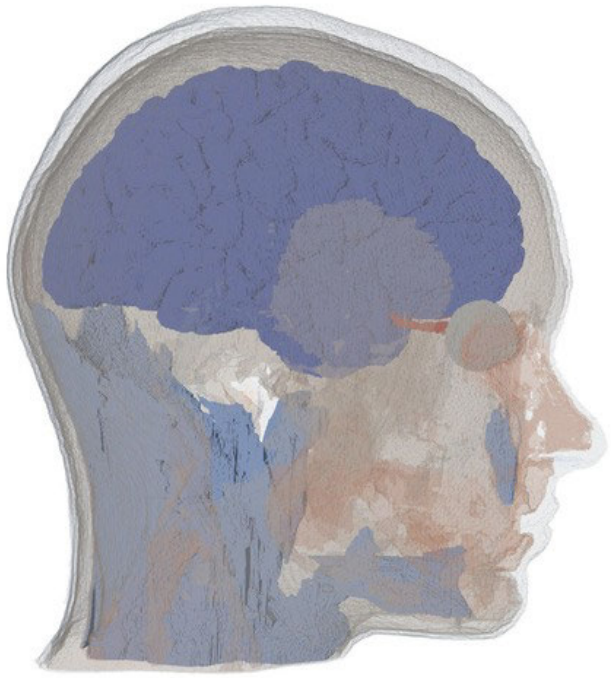

Fig. 1. The Mida heterogenous computational head model [31] utilized in the simulations.

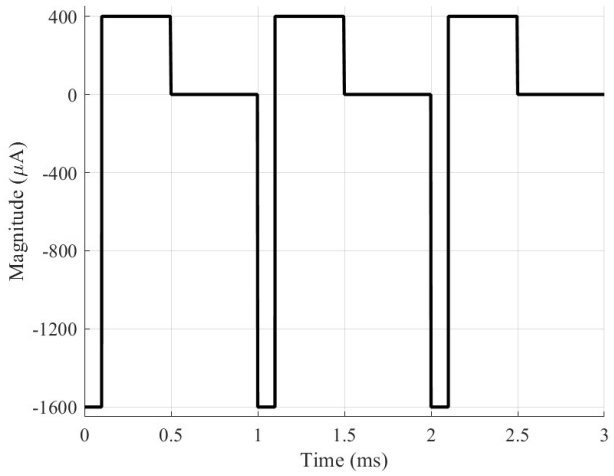

Fig. 2. Asymmetric, biphasic, input current in cadaveric ex-vivo induced voltage measurement.

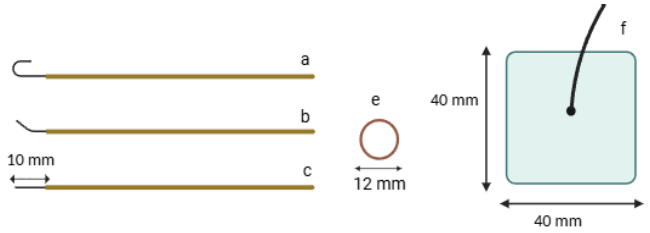

Fig. 3. Stimulation and ground electrodes used for EF-guided optic nerve regeneration. a) J stimulation electrode with 30 mm length b) L-shaped endonasal ground electrode with 10 mm length c) intracranial needle electrode ground with 10 mm length e) contact lens stimulation electrode with 6 mm radius f) plate ground electrode with 40 mm length of each edge (Created in BioRender. Simonyan, A. (2024) https://BioRender.com/y98g919).

our model with measurements from cadaveric heads which do not possess fluids, such as cerebrospinal fluid (CSF), we also generated a model in which locations normally filled with CSF were replaced with neighboring white matter (WM). This was performed because it was assumed that, in cadaver heads, CSF spaces are collapsed and "filled" with WM tissue.

D. Electrical Input/Waveform

The stimulation method is current controlled with an input current of 400 μA. The anodic phase of the biphasic waveform shown in Fig. 2 was used as the input current in simulations. The rationale for this choice, detailed in the section II-F, is based on its dominant role in promoting axonal growth, as supported by findings in [1], [5], [17].

E. Cadaveric Surgery

We validated our computational model by performing voltage gradient measurements in cadaveric heads (University of California San Diego Body Donation Program). Electrodes used for stimulation are shown in Fig. 3 and fabricated according to specifications listed in Section II-B.

The contact lens electrode (ERG jet electrode, Diagnosys, Lowell, USA) was placed on the corneal surface and secured with partial thickness scleral bites using 6-0 vicryl suture (Ethicon, Raritan, NJ). The J, needle, and endonasal electrodes were custom-made using tungsten wire with a 1 mm diameter, covered in heat shrink wrap, and selectively exposed as specified in Section II-B. The plate electrode is made from stainless steel.

The orbit was then accessed by performing a 360 circumferential limbal peritomy. The optic nerve was identified temporally by carefully reflecting the muscle cone and surrounding orbital fat. The J electrode was placed under the lateral rectus around the optic nerve; the distal end was secured to the orbit at the lateral canthus with 4-0 silk (Ethicon, Raritan, NJ).

To obtain access to the orbital apex, we performed an extended endoscopic endonasal transsphenoidal approach, removing the lamina papyracea, the optic protuberance, sellar floor, and tuberculum sella to expose the optic nerve and chiasm. The endonasal electrode was placed endoscopically through the nasal cavity along the optic nerve and secured into place with Adherus dural sealant (Stryker, Kalamazoo, USA). To obtain access to the skull base, we performed a standard pterional craniotomy to gain access to the optic nerve and chiasm. A needle-shaped intracranial electrode was placed inside the optic tract contralateral to the eye with the contact lens electrode.

A midline scalp incision was made, the scalp lifted off the skull with a freer elevator. The plate electrode, which was made by soldering a 100 mm copper wire (18 gauge) to a 40 mm x 40 mm stainless steel plate with 254 μm thickness (SAW 304) was positioned over the occipital bone. The wire electrode was threaded through a small incision made in the scalp. The scalp was then sutured together with 4-0 silk to prevent electrode movement.

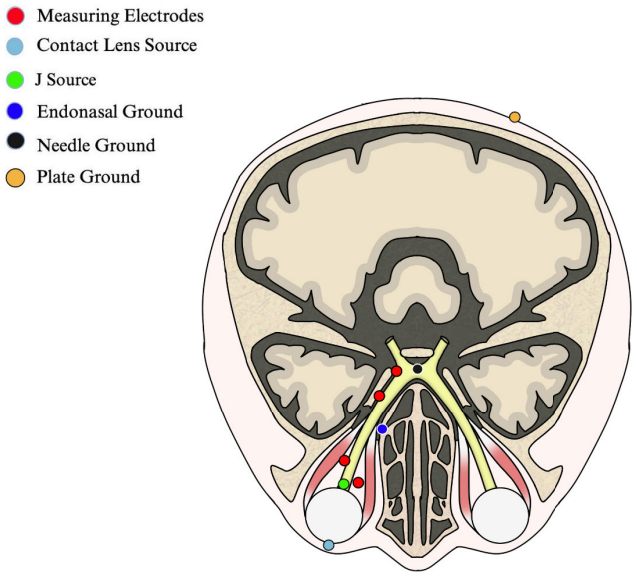

Fig. 4. Location of measuring electrodes, stimulation electrodes and ground electrodes in cadaveric experiments to measure induced voltage along the optic nerve (Created in BioRender. Simonyan, A. (2024) https://BioRender.com/y98g919).

Measuring electrodes were placed along the anterior visual pathway. Specifically, an 11 blade was used to carefully puncture a small hole 1mm behind the temporal limbus. Two measuring electrodes were placed in series along the optic nerve, one behind the globe which was secured while the second was placed deep in the orbit at the orbital apex. 2 more measuring electrodes were placed along the ipsilateral and contralateral optic tracts. All electrodes were secured into place to the dura with 4-0 silk to prevent movement. A schematic of the electrode's location is shown in Fig. 4.

F. Voltage Measurements

For stimulation, we utilized the MCS stimulus generator (STG 4008, Harvard Bioscience, Holliston, USA) in continuous current mode [41]. The input current is an asymmetric charge-balanced biphasic waveform with a frequency of 1 kHz, as depicted in Fig. 2. This current mirrors the one found to be effective during in-vivo experiments with rats [18]. In this case, however, the amplitude was increased fourfold for both anodic and cathodic phases. The rationale for selecting this amplitude in humans is based on the relationship between current amplitude used for deep brain stimulation in rats versus humans. As reported in [42], currents up to 400 μA were examined, with humans typically requiring 3-5 times this amplitude. Current was delivered via alligator clamps attached to each electrode.

The grounds of the stimulator and the oscilloscope are connected together and also linked to the ground electrode, with the measurement performed in a single-ended configuration.

Voltage measurements were performed utilizing deep brain stimulation (DBS) probes (2 DB-2202-45 and 2 DB-2201-45DC, Boston Scientific, Marlborough, USA). The DB-2202-45 model features 4 contacts spaced 2 mm apart, whereas the DB-2201-45DC model includes 8 contacts, also with a 2 mm spacing between each [43], [44], [45]. In DB-2201-45DC, 4 contacts are used interchangeably, making the distance between measurement points equal to 4 mm. As shown in Fig. 4, two electrodes are located along the ON in the orbit, while two other electrodes are located along the ON after the orbit. Measurements were performed bilaterally on three cadaveric heads, totaling six eyes (N = 6).

We used a DSOX2014A oscilloscope (Keysight, Santa Rosa, USA) with 10X probes for monitoring and recording the voltage, together with a custom switching circuit realized with one Arduino uno (Arduino, Monza, Italy) and 4 multiplexers (74HC4051) so as to be able to measure 16 points. We report the anodic component only as this is the phase that has been shown to be effective at driving axon growth [5], [17], [18].

III. Results

A. Cadaveric Conductivity Measurements

We measured the conductivity of white matter, gray matter, muscle, fat, cornea, sclera, vitreous humor, lens and optic nerve as described in Section II-A. Table I compares the measured values with those provided by IT'IS in [25], which are based on Gabriel dispersion and IT'IS low frequency conductivity values. Coefficient of variation (CV), defined as the standard deviation divided by the arithmetic mean, was used to compare the measurements. The CV was used to account for the different scaling of the tissue properties. The highest CV in conductivity was observed in white matter and fat tissues.

B. Computational Modeling of Induced Fields

Fig. 5 shows the simulated voltage distribution at the orbitomeatal plane for 6 different electrode configurations, as obtained using the AM method described in Section II-C and D. In these experiments, simulations with (left) and without CSF (right) were performed. Simulations without CSF were performed as we hypothesized that these would more closely mimic our cadaveric experiments and would allow for a more accurate validation of our findings.

The highest voltage is at the stimulation electrodes, and the lowest is near the ground electrodes, for both models (with and without CSF). The voltage, as expected, drops to zero at the ground electrodes; this, however, does not show in Fig. 5 ac, ad, bc and bd as the endonasal ground is located at a different plane than that in the figures.

As described in our previous work [16], the potential for guided optic nerve regeneration is tied to the voltage distribution along the optic nerve. Fig. 6 shows such simulated voltage distribution for both cases in which the computational model includes CSF or does not include CSF. Simulations show that the electrode most impacted by the presence of CSF is the intracranial needle ground which terminates at the chiasm, an area surrounded by the CSF.

EF for the same models is plotted in Fig. 7. Once again, the intracranial needle electrodes are the most impacted by the presence or absence of CSF; this affects in particular the field intensity in the region proximal to the ground. Notably, absence of CSF increases the EF around the needle ground electrode by almost 100%.

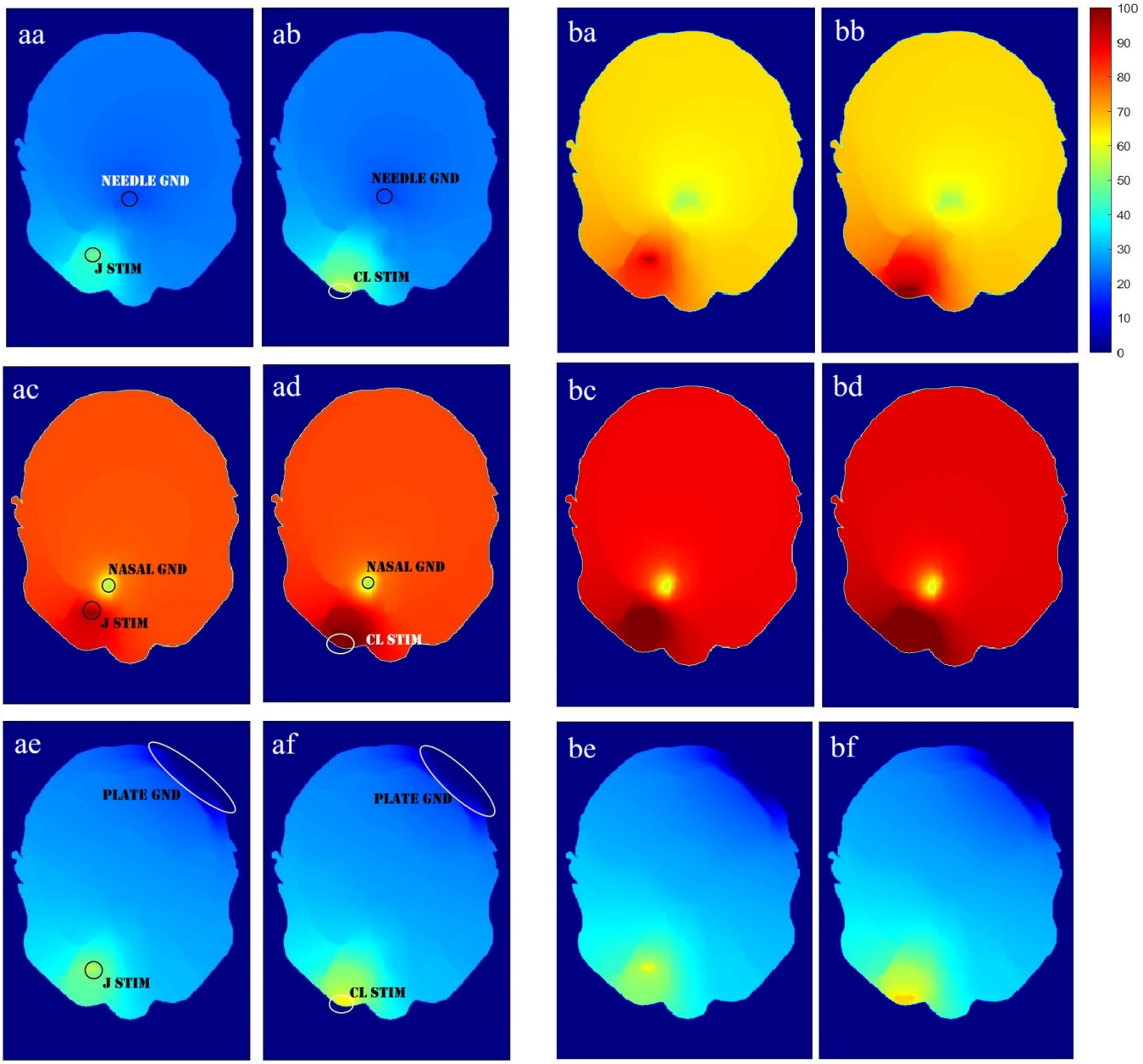

Fig. 5. Computed voltage (mV) distribution at the orbitomeatal plane for aa) J stimulation – needle ground, ab) Contact lens stimulation – needle ground, ac) J stimulation – nasal ground, ad) Contact lens stimulation – nasal ground, ae) J stimulation – Plate ground, af) Contact lens stimulation - Plate ground, performed including CSF to recapitulate the fields induced in the head of a potential patient. Computed voltage (mV) distribution at the orbitomeatal plane performed with replacing CSF with white matter to recapitulate the fields induced in a cadaver head in ba) J stimulation – needle ground, bb) Contact lens stimulation – needle ground, bc) J stimulation – nasal ground, bd) Contact lens stimulation – nasal ground, be) J stimulation – Plate ground, bf) Contact lens stimulation - Plate ground configurations.

When using a CL electrode instead of the J electrode as the source, the induced EF decreases. There are two important observations that can be made about this difference. First, in all conditions, the largest decrease in EF occurs at the optic disc (where the optic nerve leaves the eye, i.e., $x = 0$). In Fig. 7, this decrease continues until 20 mm away, after which the EF along the optic nerve is the same for both J and contact lens stimulation. Secondly, pairing the CL with the endonasal ground decreases the EF by 62% compared to the J with endonasal. This difference between CL and J when paired with either needle or plate grounds is 71%. This suggests that, as the ground gets farther from the stimulation electrode, the effect of the contact lens electrode becomes more significant but, eventually, this effect stabilizes. The same observations apply to the case without CSF.

When comparing different grounds, the endonasal ground produces the largest EF along the optic nerve, followed by the needle and then the plate. This was expected, as the EF between two electrodes decreases as the distance between them increases.

C. Cadaveric Voltage Measurements

To validate the results provided by the simulations, measurements in cadaveric heads were performed as described in

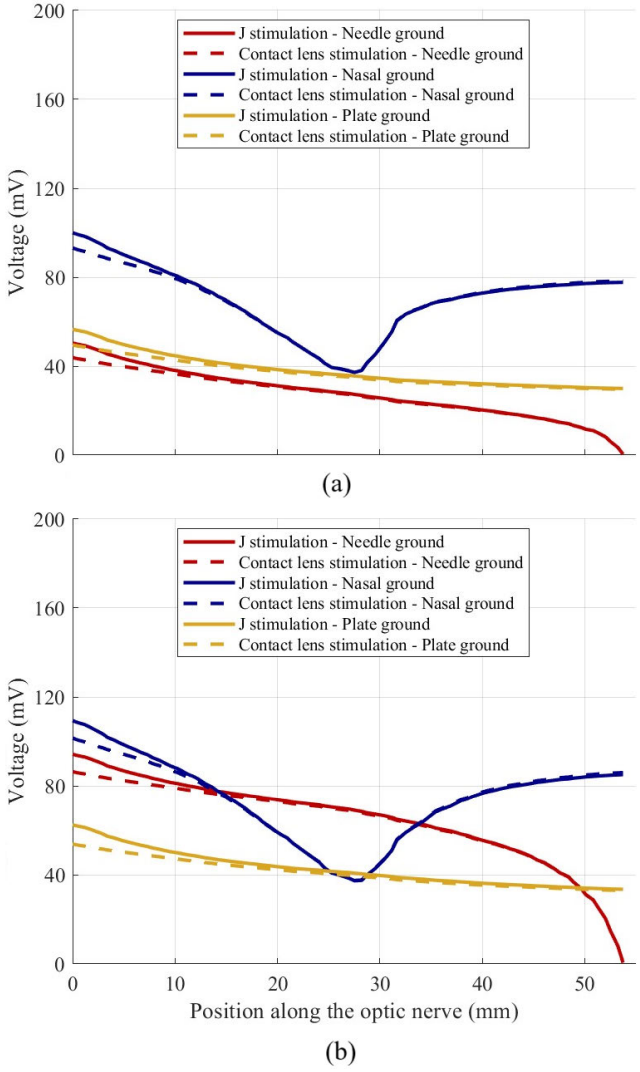

Fig. 6. Simulated voltage along the ON of a human model for different combinations of direct and indirect stimulation and ground electrodes. a) With CSF. b) Without CSF. Stimulation is with a current source of amplitude 400 μA.

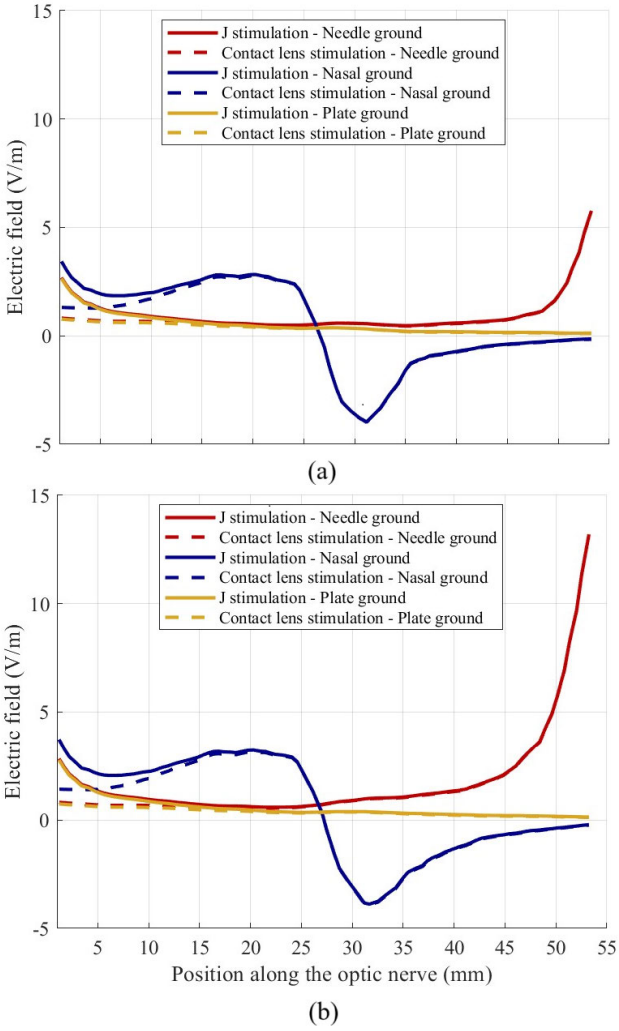

Fig. 7. Simulated electric field along the ON of a human model for different combinations of direct and indirect stimulation and ground electrodes. a) With CSF. b) Without CSF. Stimulation is with a current source of amplitude 400 μA.

Section II-E and F. The measured voltages at several locations on the optic nerve are shown in Fig. 8. To mitigate the coarseness of the measured voltage, we adopted a curve fitting procedure.

Fig. 9 compares the measured electric field (determined from the fitted curve of the measured voltage) to the simulated electric field. The results show a general consistency in values and profiles between measurement and simulation, particularly given the significant anatomical differences between the computational model of the human head and cadaveric heads. As noted earlier, the absence of CSF had the greatest impact on cases with the intracranial needle ground electrode; indeed, those measurements are in better agreement with simulations performed without CSF than with CSF. Consistent with our simulations, measurements in cadavers demonstrate that using a CL stimulation electrode reduces the EF, with the maximum reduction observed at the optic disc. Furthermore, the endonasal ground produces the highest EF, while the plate ground generates the lowest.

IV. Discussion

This paper presents an important step towards the development of a wearable or minimally invasive system to aid in the regeneration of axons of the optic nerve. Currently, over 60 million patients worldwide are legally blind from glaucoma, a painless neurodegenerative disease characterized by gradual loss of RGCs that occurs over decades. Vision loss in these patients is permanent, associated with increased falls and revocation of driving privileges with end stage disease. Development of a wearable device that could deliver treatment daily to slow or even reverse RGC degeneration is needed to reduce the morbidity associated with this disease. The premise for our investigation is based on the finding that application of asymmetric biphasic stimulation waveforms to the optic nerve described in [17] is effective at driving directional regeneration of damaged RGC axons. Electrode configurations evaluated to date were performed in rats and demonstrated to be effective at mediating partial anatomical and electrophysiological restoration. This work employed a source electrode implanted behind the eye (J electrode) and a

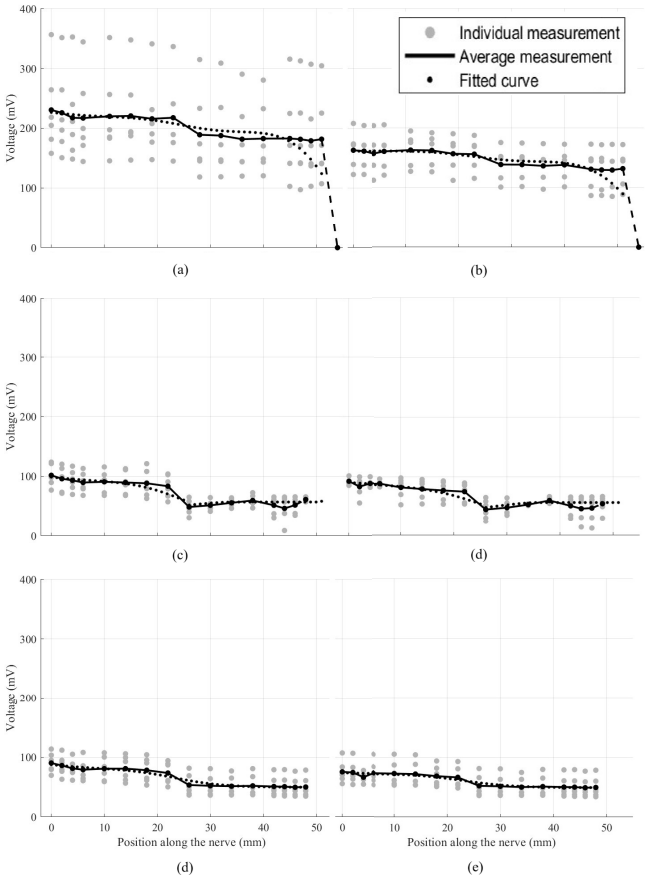

Fig. 8. Measured voltage along the optic nerve of human cadavers, total of 6 measurements (Gray dots), the average (Black dots and line) and the fitted curve to the average measurement (small black dots) a) J stimulation – needle ground. b) Contact lens stimulation – needle ground. c) J stimulation – nasal ground. d) Contact lens stimulation – nasal ground. e) J stimulation – Plate ground. f) Contact lens stimulation - Plate ground.

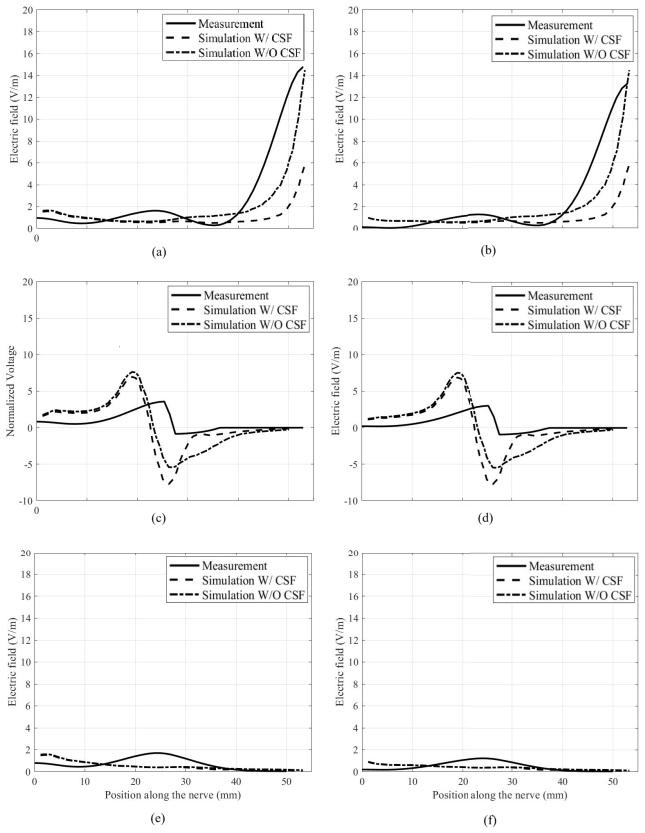

Fig. 9. Measured electric field along the optic nerve (curve-fitted, from 6 experimental measurements) compared against simulated electric field in a heterogeneous human head model, with and without CSF. The graphs correspond to the following configuration (stimulation electrode-ground electrode): (a) J-needle; b) Contact lens-needle; c) J-nasal; d) Contact lens-nasal; e) J-plate; f) Contact lens-plate.

needle ground into the contralateral optic tract. If efficacy can be shown using minimally invasive stimulation devices—such as a contact lens paired with a scalp electrode—even if their effectiveness is somewhat lower than that of implanted J and intracranial electrode combinations, the impact on the field of neuro-restoration could be significant, given the potentially improved safety profile of these surface electrodes.

Translating rodent findings to the human will invariably require more investigation than just scaling electrode size. Thus, we developed and validated a computational model of electrical stimulation of the human head, both with CSF and without CSF, to be used as a tool by the community to streamline device design. While we modeled endonasal, intracranial, or scalp electrodes as ground electrodes, any number of electrodes with various shapes in different positions can be tested with our model to determine the optimal placement of electrodes and their configuration. Our findings show that simulations closely resemble measurements in cadavers, with significant differences arising only when electrodes are positioned within the cerebrospinal fluid (CSF).

Our experiments show that the contact lens stimulating electrode produces smaller fields at the level of the optic disc (the region on the retina where optic nerve fibers converge and exit the eye) compared to those of the J electrode, regardless of the chosen ground. The reason for this is that the EF decreases rapidly with all electrode configurations. In the case of the CL electrode, the EF is already low by the time it reaches the optic nerve head, whereas with the J electrode, the EF is greatest at the nerve head.

Given that in diseases like glaucoma and ischemic optic neuropathies cause damage to RGC axons at the optic nerve head, the low field strength generated in this region by CL electrodes raises the question of whether a wearable stimulating electrode can be effective. However, since the CL electrode has a larger surface area than the J electrode, it is also likely to allow delivery of a higher safe current based on the Shannon criteria [46]. Thus, it may be possible to compensate for the reduced EF by increasing the input current. This hypothesis is currently under active investigation by our group.

Another important factor in the electrical stimulation of the optic nerve is that the position and shape of the ground electrode significantly affect the field distribution. For instance, the plate electrode consistently generates the lowest EF, regardless of the paired stimulation source. This outcome could be attributed to the distance between the stimulation and ground electrodes or the large size of the plate. However, since the endonasal and needle electrodes are the same size, yet the needle consistently produces a lower EF than the

endonasal electrode, the most plausible explanation is that the distance between the electrodes, rather than their size, has the greatest influence on EF amplitude.

Configurations that can minimize the distance between the stimulating and ground electrodes are more likely to be more effective at directing axon growth. While the endonasal ground presents as an attractive solution to this problem, given ease of placement by a skilled neurosurgeon, it is important to note that the EF direction behind the endonasal electrode (towards the brain) is negative, which is undesirable for axon regeneration as it would direct axon growth back to the eye. To address this, the endonasal electrode would also need to be used as the stimulation electrode and paired with another downstream electrode, such as a needle or plate, as the ground. In other words, electrodes would likely need to be activated in series to drive axon growth.

It should be noted that, for the measurements in cadaveric heads, electrodes could not be removed after being positioned. For example, the endonasal ground electrode was left in position but disconnected when not in use. The presence of the metallization, although disconnected, could have had a minor effect on the results, as evidenced by the undulation of the measured electric field around the 20 mm point (location of the disconnected endonasal electrode) in the cases of needle and plate electrodes.

Although factors such as contact surface area, local tissue conductivity, and mechanical pressure from surrounding tissue or electrode placement can influence measured values, substantial efforts were made to minimize surgical variability across experiments. As a result, recorded voltages exhibited consistent trends, indicating that, while some variability is present, it does not undermine the reliability of our findings. The sensitivity of the electric field (EF) distribution to tissue property variability was further assessed through simulations in which dielectric properties were systematically varied. For instance, altering the conductivity of gray and white matter by $+/-$ 10% led to less than a 5% change in EF amplitude across different electrode configurations. These results indicate that moderate uncertainties in tissue conductivity have a limited effect on the EF distribution.

For our conductivity measurements, the highest variation was observed for fat and white matter. Since fat has a very low conductivity, we hypothesize that any water present in or around the fat causes the conductivity to jump unpredictably, as the water provides a small channel for ions to flow. In higher conductivity tissues, the conductivity difference between the tissue and fluids present is not as drastic, leading to smaller measurement variations. This hypothesis is corroborated by the work of Jones et al. [47], in which it was found that a surface layer of liquid can drastically affect the measurement on low conductivity tissues. In addition, the conductivity of white matter had particularly high variation due to its anisotropy, which was not accounted for in the measurement.

When modeling EF stimulation of the visual pathway, we attempted to closely recapitulate our experimental setup by removing CSF from our computational models. While this appeared to be impactful for intracranial electrodes or electrodes that are located in space normally filled with CSF, little effect was noted when surface electrodes were modeled. Thus, when designing wearable surface electrodes, CSF properties appear to play a secondary role in estimating the EF that is induced in the human head. Furthermore, measurements in cadavers appear to be adequate for estimating EFs induced in the head using surface electrodes.

In summary, our quasistatic simulations are a viable tool for designing and testing electrode configurations that can be used to establish target induced fields in the optic nerve. This work validates the approach of utilizing such simulations for future studies of clinically relevant configurations for optic nerve growth, including the pursuit of multi-electrode configuration or possibly the employment of inversion algorithms to determine electrode configurations necessary to achieve a desired induced electric field.

V. Conclusion

In this study, we explored implanted and minimally invasive approaches for guided optic nerve regeneration by leveraging computational modeling and experimental validation. Our work demonstrates the feasibility of generating targeted electric fields conducive to axonal growth, with simulations verified through measurements in cadavers. Results highlight the critical role of electrode placement and design, with configurations such as the endonasal ground showing promise for achieving effective field distributions. The computational model developed and validated in this research provides a robust tool for predicting electric field behavior and optimizing electrode configurations. The strong alignment between simulations and measurements, particularly under experimental conditions without cerebrospinal fluid (CSF), underscores the accuracy and reliability of the model. Additionally, the findings emphasize the influence of electrode geometry and position on electric field strength and direction, offering valuable insights for advancing therapeutic applications. These findings lay the groundwork for future investigations into multi-electrode systems and adaptive stimulation paradigms to enhance field uniformity and efficacy. Moving forward, integrating these results into in-vivo models will be critical for evaluating the biological outcomes and safety of the proposed methods. Further exploration of strategies to address field localization and variability across tissue types will also be essential for clinical translation.

Acknowledgment

The authors would like to express their deepest gratitude to the patients and their families who have chosen to donate their bodies for research purposes. Their contributions are vital to advancing medical science and developing treatments that bring hope to others. They also gratefully acknowledge Michael Han for his assistance in generating a new figure, which improved the visual clarity and overall quality of the article.

REFERENCES

[1] K. K. Park et al., "Promoting axon regeneration in the adult CNS by modulation of the PTEN/mTOR pathway," *Science*, vol. 322, no. 5903, pp. 963–966, Nov. 2008.

[2] J. Zhang, D. Yang, H. Huang, Y. Sun, and Y. Hu, "Coordination of necessary and permissive signals by PTEN inhibition for CNS axon regeneration," *Frontiers Neurosci.*, vol. 12, p. 558, Aug. 2018.

[3] L. Zhang, Z. Li, L. Mao, and H. Wang, "Circular RNA in acute central nervous system injuries: A new target for therapeutic intervention," *Frontiers Mol. Neurosci.*, vol. 15, Mar. 2022, Art. no. 816182.

[4] F. Sun et al., "Sustained axon regeneration induced by co-deletion of PTEN and SOCS3," *Nature*, vol. 480, no. 7377, pp. 372–375, Dec. 2011.

[5] T. Kim et al., "Electric field stimulation directs target-specific axon regeneration and partial restoration of vision after optic nerve crush injury," *PLoS ONE*, vol. 20, no. 1, Jan. 2025, Art. no. e0315562.

[6] M. S. Humayun et al., "Visual perception in a blind subject with a chronic microelectronic retinal prosthesis," *Vis. Res.*, vol. 43, no. 24, pp. 2573–2581, Nov. 2003.

[7] M. Humayun, "Bipolar surface electrical stimulation of the vertebrate retina," *Arch. Ophthalmology*, vol. 112, no. 1, pp. 110–116, Jan. 1994.

[8] E. Margalit et al., "Retinal prosthesis for the blind," *Surv. ophthalmology*, vol. 47, no. 4, pp. 335–356, 2002.

[9] K. Stingl et al., "Interim results of a multicenter trial with the new electronic subretinal implant alpha AMS in 15 patients blind from inherited retinal degenerations," *Frontiers Neurosci.*, vol. 11, p. 445, Aug. 2017.

[10] R. Eckmiller, "Learning retina implants with epiretinal contacts," *Ophthalmic Res.*, vol. 29, no. 5, pp. 281–289, 1997.

[11] K. Stingl et al., "Subretinal visual implant alpha IMS–clinical trial interim report," *Vis. Res.*, vol. 111, pp. 149–160, Jun. 2015.

[12] E. Bloch, Y. Luo, and L. da Cruz, "Advances in retinal prosthesis systems," *Therapeutic Adv. Ophthalmol.*, vol. 11, Jan. 2019, Art. no. 2515841418817501.

[13] T. Fujikado, "Retinal prosthesis by suprachoroidal-transretinal stimulation (STS), Japanese approach," in *Artificial Vision: A Clinical Guide*. Cham, Switzerland: Springer, 2017, pp. 139–150.

[14] C. Gall et al., "Alternating current stimulation for vision restoration after optic nerve damage: A randomized clinical trial," *PLoS ONE*, vol. 11, no. 6, Jun. 2016, Art. no. e0156134.

[15] V. Gaillet et al., "Optic nerve intraneural stimulation allows selective visual cortex activation," *bioRxive*, May 2018, Art. no. 311035.

[16] M. Peng et al., "Electric fields direct full-length optic nerve regeneration and partial restoration of visual function," *Investigative Ophthalmology & Vis. Sci.*, vol. 63, no. 7, p. 1139, 2022.

[17] M. G. Peng et al., "Asymmetric charge balanced waveforms direct retinal ganglion cell axon growth," *Sci. Rep.*, vol. 13, no. 1, p. 13233, Aug. 2023.

[18] K. K. Gokoffski, X. Jia, D. Shvarts, G. Xia, and M. Zhao, "Physiologic electrical fields direct retinal ganglion cell axon growth in vitro," *Investigative Opthalmol. Vis. Sci.*, vol. 60, no. 10, pp. 3659–3668, Aug. 2019.

[19] J. Paknahad, M. Machnoor, G. Lazzi, and K. K. Gokoffski, "The influence of electrode properties on induced voltage gradient along the rat optic nerve," *IEEE J. Electromagn., RF Microw. Med. Biol.*, vol. 6, no. 3, pp. 321–330, Sep. 2022.

[20] IT'IS Foundation. *Dielectric Properties*. Accessed: Oct. 25, 2024. [Online]. Available: https://itis.swiss/virtual-population/tissue-properties/database/dielectric-properties

[21] IFAC. *Dielectric Properties of Body Tissues*. Accessed: Oct. 25, 2024. [Online]. Available: http://niremf.ifac.cnr.it/tissprop/htmlclie/htmlclie.php

[22] J. Zimmermann and U. van Rienen, "Ambiguity in the interpretation of the low-frequency dielectric properties of biological tissues," *Bioelectrochemistry*, vol. 140, Aug. 2021, Art. no. 107773.

[23] I. Kuznetcov, A. Kantzas, and S. Bryant, "Dielectric spectroscopy of nanofluids in deionized water: Method of removing electrode polarization effect," *Colloids Surf. A, Physicochemical Eng. Aspects*, vol. 647, Aug. 2022, Art. no. 129039.

[24] I. Miccoli, F. Edler, H. Pfnür, and C. Tegenkamp, "The 100th anniversary of the four-point probe technique: The role of probe geometries in isotropic and anisotropic systems," *J. Phys., Condens. Matter*, vol. 27, no. 22, Jun. 2015, Art. no. 223201.

[25] IT'IS Foundation. *Low Frequency Conductivity*. Accessed: Jan. 2025. [Online]. Available: https://itis.swiss/virtual-population/tissue-properties/database/low-frequency-conductivity/

[26] C. Gabriel and S. Gabriel, "Compilation of the dielectric properties of body tissues at RF and microwave frequencies," Dept. Phys., King's College London, London, U.K., Tech. Rep. AL/OE-TR-1996-0037, 1996.

[27] S. K. Agadagba, L. W. Lim, and L. L. H. Chan, "Advances in transcorneal electrical stimulation: From the eye to the brain," *Frontiers Cellular Neurosci.*, vol. 17, Mar. 2023, Art. no. 1134857.

[28] S. K. Agadagba, A. B. M. Eldaly, and L. L. H. Chan, "Transcorneal electrical stimulation induces long-lasting enhancement of brain functional and directional connectivity in retinal degeneration mice," *Frontiers Cellular Neurosci.*, vol. 16, Feb. 2022, Art. no. 785199.

[29] A. Gonzalez Calle et al., "An extraocular electrical stimulation approach to slow down the progression of retinal degeneration in an animal model," *Sci. Rep.*, vol. 13, no. 1, p. 15924, Sep. 2023.

[30] G. M. Noetscher, J. Yanamadala, S. N. Makarov, and A. Pascual-Leone, "Comparison of cephalic and extracephalic montages for transcranial direct current stimulation—A numerical study," *IEEE Trans. Biomed. Eng.*, vol. 61, no. 9, pp. 2488–2498, Sep. 2014.

[31] IT'IS Foundation. *Mida Model*. Accessed: Aug. 8, 2024. [Online]. Available: https://itis.swiss/virtual-population/regional-human-models/mida-model/

[32] C. J. Cela, "A multiresolution admittance method for large-scale bioelectromagnetic interactions," Ph.D. dissertation, Dept. Elect. Eng., North Carolina State Univ., Raleigh, NC, USA, 2010.

[33] M. Eberdt, P. K. Brown, and G. Lazzi, "Two-dimensional SPICE-linked multiresolution impedance method for low-frequency electromagnetic interactions," *IEEE Trans. Biomed. Eng.*, vol. 50, no. 7, pp. 881–889, Jul. 2003.

[34] V. Singh et al., "Computation of induced current densities in the human body at low frequencies due to contact electrodes using the ADI-FDTD method," *IEEE Trans. Electromagn. Compat.*, vol. 52, no. 3, pp. 537–544, Aug. 2010.

[35] D. T. Brocker and W. M. Grill, "Principles of electrical stimulation of neural tissue," in *Handbook of Clinical Neurology*, vol. 116. Amsterdam, The Netherlands: Elsevier, 2013, pp. 3–18.

[36] C. S. Bingham et al., "Admittance method for estimating local field potentials generated in a multi-scale neuron model of the hippocampus," *Frontiers Comput. Neurosci.*, vol. 14, p. 72, Aug. 2020.

[37] K. Loizos, R. Marc, M. Humayun, J. R. Anderson, B. W. Jones, and G. Lazzi, "Increasing electrical stimulation efficacy in degenerated retina: Stimulus waveform design in a multiscale computational model," *IEEE Trans. Neural Syst. Rehabil. Eng.*, vol. 26, no. 6, pp. 1111–1120, Jun. 2018.

[38] K. Loizos et al., "A multi-scale computational model for the study of retinal prosthetic stimulation," in *Proc. 36th Annu. Int. Conf. IEEE Eng. Med. Biol. Soc.*, Aug. 2014, pp. 6100–6103.

[39] K. Loizos, "A multiscale computational modeling platform for design and analysis of electrical neural stimulation," Ph.D. thesis, Dept. Elect. Eng., The Univ. Utah, Salt Lake City, UT, USA, 2017.

[40] C. S. Bingham, "Simulating electrical stimulation and recording in a multiscale model of the hippocampus," Ph.D. dissertation, Dept. Elect. Eng., The Univ. Sothern California, Los Angeles, CA, USA, 2019.

[41] Warner Instruments. *(STG4000 Series) MCS Stimulus Generators*. Accessed: Jan. 2025. [Online]. Available: https://www.multichannelsystems.com/sites/multichannelsystems.com/files/documents/brochures/STG4000_STG3008-FA-Brochure.pdf

[42] C. Hamani, M. Diwan, S. Isabella, A. M. Lozano, and J. N. Nobrega, "Effects of different stimulation parameters on the antidepressant-like response of medial prefrontal cortex deep brain stimulation in rats," *J. Psychiatric Res.*, vol. 44, no. 11, pp. 683–687, Aug. 2010.

[43] *VerciseT Deep Brain Stimulation Systems Product Catalogue*, Boston Scientific, Marlborough, MA, USA, 2020.

[44] Boston Scientific Corporation. (2019). *Summary of Safety and Effectiveness Data (SSED)*. [Online]. Available: https://www.accessdata.fda.gov/cdrh_docs/pdf15/P150031S028B.pdf

[45] Boston Scientific Corporation. *VerciseT Deep Brain Stimulation Systems-Surgical Implant Manual*. Accessed: Jan. 2025. [Online]. Available: https://www.bostonscientific.com/content/dam/elabeling/nm/92328632-05B_DBS_Surgical_Implant_Manual_US_EN_s.pdf

[46] R. V. Shannon, "A model of safe levels for electrical stimulation," *IEEE Trans. Biomed. Eng.*, vol. 39, no. 4, pp. 424–426, Apr. 1992.

[47] D. M. Jones, R. H. Smallwood, D. R. Hose, and B. H. Brown, "Constraints on tetrapolar tissue impedance measurements," *Electron. Lett.*, vol. 37, no. 25, pp. 1515–1517, Dec. 2001.